Investigation of the Linear and Nonlinear Optical Susceptibilities of KTiOPO4 Single Crystals: Theory and Experiment

ARTICLE *in* THE JOURNAL OF PHYSICAL CHEMISTRY B · DECEMBER 2010

Impact Factor: 3.3 · DOI: 10.1021/jp1072878 · Source: PubMed

3 AUTHORS:

Ali H Reshak
University of West Bohemia
477 PUBLICATIONS **3,425** CITATIONS
SEE PROFILE

Iwan V Kityk
Czestochowa University of Technology
961 PUBLICATIONS **7,943** CITATIONS
SEE PROFILE

Sushil Auluck
Indian Institute of Technology Kanpur
313 PUBLICATIONS **3,092** CITATIONS
SEE PROFILE

Investigation of the Linear and Nonlinear Optical Susceptibilities of $KTiOPO_4$ Single Crystals: Theory and Experiment

Ali Hussain Reshak,*,†,‡ I. V. Kityk,§ and S. Auluck||

Institute of Physical Biology-South Bohemia University, Nove Hrady 37333, Czech Republic, School of Microelectronic Engineering, University Malaysia Perlis (UniMAP), Block A, Kompleks Pusat Pengajian, 02600 Arau Jejawi, Perlis, Malaysia, Electrical Engineering Department, Czestochowa University of Technology, Al.Armii Krajowej 17/19, Czestochowa, Poland, and National Physical Laboratory, Dr. K S Krishnan Marg, New Delhi 110012, India

Received: August 3, 2010; Revised Manuscript Received: October 21, 2010

Experimental and theoretical studies of the linear and nonlinear optical susceptibilities for single crystals of potassium titanyl phosphate $KTiOPO_4$ are reported. The state-of-the-art full potential linear augmented plane wave method, based on the density functional theory, was applied for the theoretical investigation. The calculated direct energy band gap at Γ, using the Engel−Vosko exchange correlation functional, is found to be 3.1 eV. This is in excellent agreement with the band gap obtained from the experimental optical absorption spectra (3.2 eV). We have calculated the complex dielectric susceptibility $\varepsilon(\omega)$dispersion, its zero-frequency limit $\varepsilon_1(0)$ and the birefringence of $KTiOPO_4$. The calculated birefringence at the zero-frequency limit $\Delta n(0)$ is equal to about 0.07 and $\Delta n(\omega)$ at 1.165 eV ($\lambda = 1064$ nm) is 0.074. We also report calculations of the complex second-order optical susceptibility dispersions for the principal tensor components: $\chi^{(2)}_{113}(\omega)$, $\chi^{(2)}_{232}(\omega)$, $\chi^{(2)}_{311}(\omega)$, $\chi^{(2)}_{322}(\omega)$, and $\chi^{(2)}_{333}(\omega)$. The intra- and interband contributions to these susceptibilities are evaluated. The calculated total second order susceptibility tensor components $|\chi^{(2)}_{ijk}(\omega)|$ at $\lambda = 1064$ nm for all the five tensor components are compared with those obtained from our measurements performed by nanosecond Nd:YAG laser at the fundamental wavelength ($\lambda = 1064$ nm). Our calculations show reasonably good agreement with our experimental nonlinear optical data and the results obtained by other authors. The calculated the microscopic second order hyperpolarizability, β_{333}, vector component along the dipole moment direction for the dominant component $\chi^{(2)}_{333}(\omega)$ is found to be 31.6×10^{-30} esu, at $\lambda = 1064$ nm.

I. Introduction

Potassium titanyl phosphate $KTiOPO_4$ (KTP) is a nonlinear optical (NLO) single crystal that is commonly used for frequency doubling diode pumped solid-state lasers such as Nd:YAG and other neodymium-doped lasers. The crystal structure of KTP was first determined by Tordjman et al.[1] KTP has a large second order electronic dielectric constant,[2] low thermal expansion coefficient and a slow variation of the optical constants with temperature (excellent thermal stability). These facts make KTP very favorable for use as second harmonic generators of near-infrared laser light.[3−5] It is highly transparent for spectral range between 350−2700 nm with a reduced transmission up to 4500 nm where the crystal is effectively opaque.[4] Its effective second harmonic generation (SHG) coefficient is about three times higher than KDP (KH_2PO_4). It has a Mohs hardness of about 5. At the same time KTP is an inexpensive ferroelectric material belonging to the family of isomorphic nonlinear optical crystals with the general formula $MTiOXO_4$ (M = [K, Rb, Tl, Cs], X = [P, As]) and is used for electro-optic applications.[6] KTP possesses a high damage threshold (∼9.6 GW/cm^2) which makes it very useful for application in high power laser light modulation.[6] However, it is prone to photochromic damage (called gray tracking) during high-power 1064 nm second-harmonic generation that results in its limited use in low and midpower systems. The ion exchange properties of KTP make it useful in waveguide applications.[6] Stucky et al.[4] have presented an extensive review of the crystal structure and physicochemical properties of KTP and other isostructural compounds. KTP is also frequently used as an optical parametric oscillator for near IR generation up to 4 μm. It is particularly suited to high power laser light operation as an optical parametric oscillator due to its high damage threshold and large crystal aperture.[4] The high degree of birefringent walk-off between the pump signal and idler beams present in this material limits its application as an optical parametric oscillator for very low light power applications. KTP is also used as an electro-optic modulator, optical waveguide material, and in directional couplers. The research[7] illustrates another remarkable property of KTP, the large temperature window over which it can be used in NLO application.[7] Zhang et al.[8] studied the ion exchange in KTP crystals irradiated by copper and hydrogen ions. Pena et al.[9] studied a two-dimensional KTP photonic crystal grown using a macroporous silicon template. One of the most important applications is a laser system for medical surgery that uses KTP for generating blue light.[10] However, even though decades have passed since KTP's recognition as a NLO material of choice, it is just in recent years that some significant improvements have been made regarding the true nature of the ferroelectric to paraelectric phase transition.[10] Pysher et al.[11] used KTP to generate −2.2 dB of broadband amplitude squeezing at 1064 nm in a periodically poled KTP waveguide by coupling of the fundamental and

* To whom correspondence should be addressed. Tel. +420 777729583. Fax. +420-386 361231. E-mail address:maalidph@yahoo.co.uk.
† Institute of Physical Biology-South Bohemia University.
‡ University Malaysia Perlis (UniMAP).
§ Czestochowa University of Technology.
|| National Physical Laboratory.

10.1021/jp1072878
Published on Web 12/02/2010

second harmonic cw fields. Kugel et al.[12] have studied KTP by Raman and infrared reflectivity spectroscopy in the range from a low temperature to room temperature at various scattering configurations.

From the above-mentioned, it is clear that there is dearth of theoretical work on KTP. As a consequence, we feel that KTP crystals may serve as a good model subject for verification of the different models of the second order susceptibilities for complex inorganic materials. Theoretical studies will be helpful in elucidating the relationship between structure and the optical susceptibilities (both linear as well as nonlinear). In the past, ab initio density functional theory (DFT) calculations have been extensively applied for the computations of structural and optical parameters. Further, the efficiency of the optical susceptibilities is inherently dependent upon the structural features. As a result, it would be valuable to probe and understand the structure and optical properties in this class of crystals. A detailed description of the optical properties of KTP crystal using a DFT full potential method is very essential and could bring important insights into understanding the origin of the electronic properties, their relations with principal structural parameters, chemical bonds and their relation with dispersion of linear and nonlinear optical constants. At the same time, we have also performed experimental measurements using Nd:YAG laser at the fundamental wavelength for measuring the second-order susceptibilities to compare them with the results of our theoretical calculations and other available experimental and theoretical results.

The experimental details are given in Section II and the computational details in Section III. Results and discussions are given in Section IV and the conclusions in Section V.

II. Experimental Details

The KTP single crystals were grown by a traditional flux method. The starting raw materials were KPO_3, H_2O, $K_4P_2O_7$, and TiO_2. The flux system content corresponded to $K_6P_4O_{13}$, which is obtained by adjusting the ratio of KPO_3 and $K_4P_2O_7$, or KH_2PO_4 and K_2CO_3. The amount of KTP was 15−20 wt % in the solution. For the crystal growth, about 400 g of the raw materials were melted and soaked in platinum crucibles (with diameter 60 mm and height 85 mm). After at least 32 h of stirring, KTP seed (with dimensions $4 \times 4 \times 25$ mm^3) was submerged into melt at a temperature 25 K higher than the saturation temperature. The temperature was decreased to the saturation temperature with rate about 0.1 K/hour. Single crystals of good quality were obtained 60 days after the seeding. Generally the crystal growth was similar to the described in the ref 13.

A routine X-ray diffraction yields lattice parameters $a = 12.817$ Å, $b = 6.408$ Å, $c = 10.612$ Å, which are in a good agreement with that reported in the literature[5,6,14−18] (see Table 1).

The quality of the samples was determined by the optically polarized methods and the space distribution of the birefringence did not exceed 10^{-5}. The main criterion of the crystal quality can be judged by the low absorption (<0.09 cm^{-1}) and the values of the refractive indices ($n^{xx}(\omega) = 1.743$, $n^{yy}(\omega) = 1.746$, and $n^{zz}(\omega) = 1.828$ at 1064 nm), which are in agreement with the reference data for these crystals[3,5,19−22] (see Table 2).

The reflection spectra were measured using a Seya Numioka vacuum monochromator with a diffraction grating possessing linear spectral resolution of 0.7 nm. The precision of the reflectivity determination was equal to about 5%. The second harmonic generation and determination of the second order susceptibilities were done using the 10 ns Nd:YAG laser generating a wavelength of 1064 nm as described in the ref 23. For this reason, the crystals were cut along the principal crystallographic axis with the varied thickness which allowed studying the desirable second order susceptibility tensor components. The pulse frequency repetitions were varied within the 1−100 Hz. As reference samples, we have used the etalon quartz crystals with known second order susceptibilities equal in our case to about 0.6 pm/V at 1064 nm.[24] The 3 GHz oscilloscope connected with fast response photodetector was used to determine the intensity of the second harmonic generation signal and the pulse width. The detection was done in the 300 different points of the sample's surface to obtain the good statistics which allow achieving the precision of the second order susceptibility evaluation equal to about 0.12 pm/V. The spectral separation between the fundamental and the second harmonic generation was performed by interferometric filters of 8 nm spectral bandwidth.

TABLE 1: Experimental and Calculated Lattice Constant of Orthorhombic (Pna21) KTP

	a (Å)	*b* (Å)	*c* (Å)
experimental	12.817,[a] 12.814,[b,e] 12.8209 (9),[c] 12.804[d]	6.408,[a] 6.404,[b] 6.4052 (6),[c] 6.404[d,e]	10.612,[a] 10.616,[b] 10.5932 (9)[e] 10.616[d]
theoretical	12.811,[f] 12.588,[g] 12.806,[h] 12.807[i]	6.403,[f] 6.293,[g] 6.399,[h] 6.400[i]	10.609,[f] 10.410,[g] 10.563,[h] 10.566[i]

[a] Reference this work, experimental. [b] Reference 15−17. [c] Reference 14. [d] Reference 5. [e] Reference 18. [f] Reference this work, theoretical (GGA-PBE). [g] Reference 6 (LDA). [h] Reference 6 (GGA-PW91). [i] Reference 6 (GGA-PBE).

TABLE 2: Calculated $\varepsilon_1^{xx}(0)$, $\varepsilon_1^{yy}(0)$, $\varepsilon_1^{zz}(0)$, $n^{xx}(\omega)$, $n^{yy}(\omega)$, $n^{zz}(\omega)$, and $\Delta n(\omega)$ Compared with the Experimental Data

	theoretical	experimental
$\varepsilon_1^{xx}(0)$	2.96[a]	
$\varepsilon_1^{yy}(0)$	2.95[a]	
$\varepsilon_1^{zz}(0)$	3.19[a]	
$n^{xx}(\omega)$	1.746[a] at (1064 nm)	1.743,[b] 1.744,[c] 1.738, [d] 1.740,[e] 1.738,[f] 1.740,[g] 1.782,[h] (at 1064 nm)
$n^{yy}(\omega)$	1.750[a] at (1064 nm)	1.746,[b] 1.748,[c] 1.745,[d] 1.746,[e] 1.745,[f] 1.743,[g] 1.790[h] (at 1064 nm)
$n^{zz}(\omega)$	1.825[a] at (1064 nm)	1.828,[b] 1.830,[c] 1.8297,[d] 1.830,[e,f] 1.830,[g] 1.868,[h] (at 1064 nm)
$\Delta n(\omega)$	0.074[a] at (1064 nm)	0.083,[b] 0.084[c] (at 1064 nm)

[a] Reference this work, theoretical. [b] Reference this work, experimental. [c] Reference 5. [d] Reference 3. [e] Reference 19. [f] Reference 20. [g] Reference 21. [h] Reference 22.

III. Computational Details

KTP crystallizes in the orthorhombic structure space group $Pna2_1$ with 64 atoms in the unit cell. The crystalline structure of KTP is shown in Figure 1. Each unit cell contains two groups of crystallographically nonequivalent KTP molecules ($Z = 8$). These two nonequivalent KTP molecules form a motif. Each unit cell contains four nonsymmetrical motifs. Four different atoms (K, Ti, O, and P) in each motif are situated in the general positions possessing the space group $Pna2_1$.[5] Therefore, each unit cell contains 2 nonequivalent Ti (Ti(1) and Ti(2)), K (K(1) and K(2)), and P (P(1) and P(2)) lattice sites, and 10 nonequivalent O (O(1), O(2), O(3), ..., O(10)) lattice sites, resulting in a total of 16 nonequivalent lattice sites in one unit cell.[5] The titanium ions have distorted octahedral coordination, each being surrounded by four phosphate groups and two oxygen ions. Each Ti ion has a short bond to an O^{2-} ion.[14]

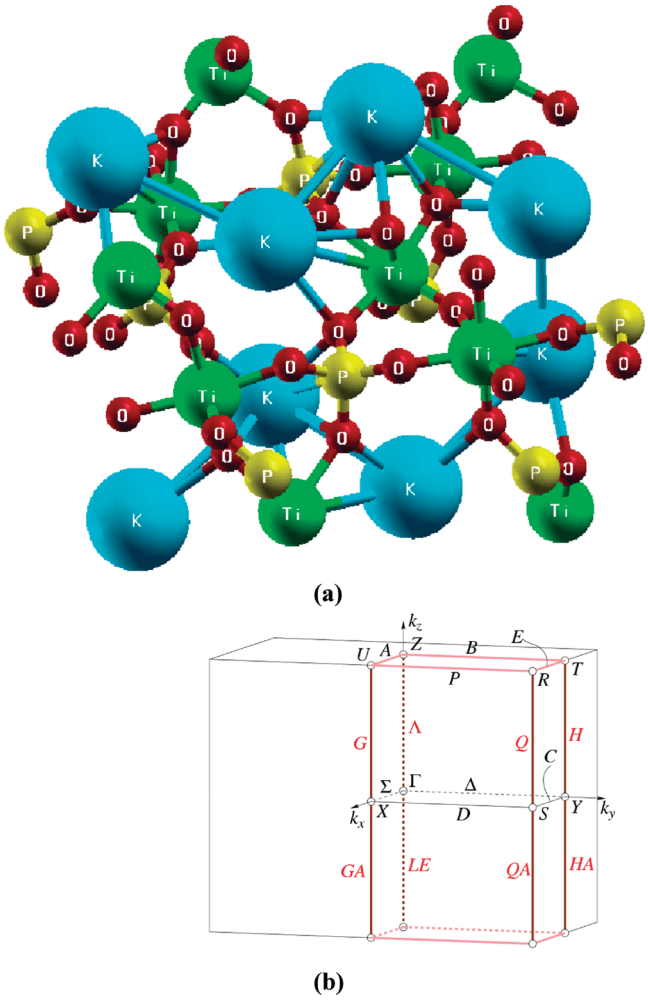

Figure 1. (a) Crystal structure of the potassium titanyl phosphate $KTiOPO_4$ (KTP) single crystal. (b) Brillouin zone.

Self-consistent calculations of the electronic structure and optical properties based on the scalar relativistic full-potential linearized augmented plane wave method (FP-LAPW) were carried out using the WIEN2K package.[25] This is a very precise and efficient approach to solve the Kohn−Sham equation within a framework of DFT. Within a framework of this approach, the potential and corresponding charge density is expanded into lattice harmonics inside each atomic sphere and as a Fourier series in the interstitial region. It is well-known that in the self-consistent band structure calculation within DFT, both the local density approximation (LDA) and the generalized gradient approximation GGA[26] approaches usually underestimate the energy gap.[27] This is mainly due to the fact that they are based on simple model assumptions, which are not sufficiently flexible to accurately reproduce the exchange correlation energy and its charge space derivative. Engel and Vosko considered this shortcoming and constructed a new functional form of GGA[28] which is able to reproduce better exchange potential at the expense of less agreement in the exchange energy by taking into account the interparticle interactions. This approach (EV-GGA) yields better band splitting compared to the GGA ones. In this work, the GGA-PBE approach[26] was used for the total energy calculations, while for the electronic structure and the optical properties the EV-GGA[28] was applied.

The Kohn−Sham equations are solved using a basis of linear APW's. To achieve energy eigenvalues convergence, the wave functions in the interstitial regions were expanded in plane waves

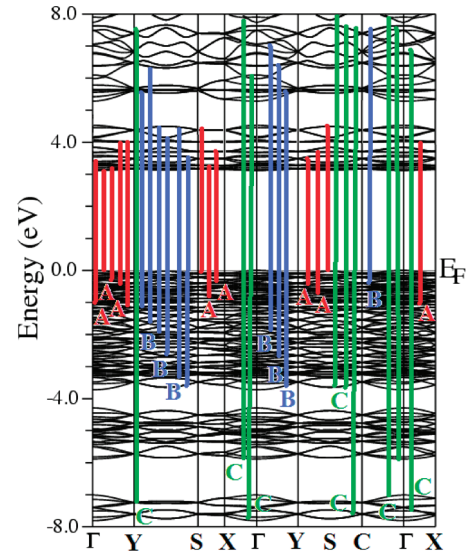

Figure 2. The optical transitions depicted on a generic band structure of the KTP .

with a cutoff $K_{max} = 9/R_{MT}$, where R_{MT} denotes the smallest atomic sphere radius and K_{max} gives the magnitude of the largest **K** vector in the plane wave expansion. The muffin-tin (MT) radii were assumed to be 1.72 atomic units (au) for Ti, 2.5 au for K, and 1.43 au for O and P atoms. The valence wave functions inside the MT were expanded up to $l_{max} = 10$ while the charge density was Fourier expanded up to $G_{max} = 14$ (au)$^{-1}$. The self-consistency was achieved using 300 k-points in the irreducible Brillouin zone (IBZ). The linear optical susceptibilities were calculated using summation over 500 k-points within the IBZ. The nonlinear optical properties were evaluated using 1200 k-points of the IBZ. The formalisms for calculating the second order susceptibility $\chi^{(2)}_{ijk}(-2\omega;\omega;\omega)$ for nonmagnetic semiconductors and insulators based on the FP-LAPW method have been presented before.[29,30] The self-consistent calculations are converged since the total energy of the system is stable within 10^{-5} Ry.

IV. Results and Discussion

A. Band Structure. We have calculated the band structure of KTP to determine the interband transitions that give rise to the major structures in the optical properties. Figure 2 shows the band structure of KTP along with the possible principal optical transitions. From our calculated band structure we found that the conduction band minimum (CBM) and valence band maximum (VBM) are located at Γ the center of the BZ resulting in a direct gap of about 3.1 eV, which is in excellent agreement with experimentally measured (3.2 eV). The agreement between the theoretical and experimental values of the energy gap is attributed to our use of FP-LAPW within EV-GGA.

B. Linear Optical Dispersion. As KTP crystallizes in the orthorhombic structure space group $Pna2_1$, the dielectric tensor has three components corresponding to the electric field $\vec{E}$ being along a, b, and c-crystallographic axes. These are the complex tensor components: $\varepsilon^{xx}(\omega)$, $\varepsilon^{yy}(\omega)$, and $\varepsilon^{zz}(\omega)$. The imaginary part of these three complex components are $\varepsilon_2^{xx}(\omega)$, $\varepsilon_2^{yy}(\omega)$ and $\varepsilon_2^{zz}(\omega)$. Measurements of the dielectric properties are normally carried out on single crystals. Sometimes experiments are performed with light vector $\vec{E}$ parallel or perpendicular to the c-axis. The experimentally determined dielectric functions are then $\varepsilon_2^{\perp}(\omega)$ and $\varepsilon_2^{\parallel}(\omega)$. These are related to the above-mentioned components by[30]

$$\frac{\varepsilon^{xx}(\omega) + \varepsilon^{yy}(\omega)}{2} = \varepsilon^{\perp}(\omega)$$

$$\varepsilon^{zz}(\omega) = \varepsilon^{||}(\omega)$$

The imaginary parts $\varepsilon_2^{xx}(\omega)$, $\varepsilon_2^{yy}(\omega)$ and $\varepsilon_2^{zz}(\omega)$ of the optical function's dispersion completely define the linear optical properties. These are shown at Figure 3a. Broadening is taken to be 0.1 eV, which is traditional for oxide crystals and is typical of the experimental accuracy. All the optical properties are scissors corrected[31] by 0.1 eV; more details about the scissors correction is give in ref 31. Basically this increases the separation between the valence and conduction bands rigidly by 0.1 eV. The scissors corrections is the difference between the calculated (3.1 eV) and measured energy gaps (3.2 eV). It is a consequence of a fact that the density functional theory calculations usually underestimate the energy gaps with respect to the experimental ones. A very simple way to overcome this drawback is to use the scissors correction factors, which merely brings the calculated energy gap close to the experimental gap.

From Figure 3a, one can see that the edge of optical absorption (fundamental absorption edge) for $\varepsilon_2^{xx}(\omega)$, $\varepsilon_2^{yy}(\omega)$ and $\varepsilon_2^{zz}(\omega)$ are located at 3.2 eV. These edges of optical absorption give the threshold for direct optical transitions between the top of valence band and bottom of conduction band. All the components $\varepsilon_2^{xx}(\omega)$, $\varepsilon_2^{yy}(\omega)$ and $\varepsilon_2^{zz}(\omega)$ display two principal peaks situated around 4.0 and 11.5 eV, respectively. Two insignificant humps are situated between these peaks around 6.0 and 8.0 eV. One can see a considerable anisotropy between these three components of the frequency dependent dielectric function. Generally a crystal, which shows a considerable anisotropy in the linear optical susceptibilities favors an enhanced phase matching conditions for the second harmonic generation (SHG) and optical parametric oscillation (OPO). To identify the spectral peaks in the linear optical spectra, we considered the optical transition matrix elements. We have used our calculated band structure to indicate the transitions, indicating the major structure for the principal components $\varepsilon_2^{xx}(\omega)$, $\varepsilon_2^{yy}(\omega)$, and $\varepsilon_2^{zz}(\omega)$ in the band structure diagram. These transitions are labeled according to the spectral peak positions in Figure 3a. For simplicity, we have labeled the transitions in Figure 2 and 3a, as A, B, and C. The transitions (A) are responsible for the structures for $\varepsilon_2^{xx}(\omega)$, $\varepsilon_2^{yy}(\omega)$ and $\varepsilon_2^{zz}(\omega)$ in the spectral range 0.0−5.0 eV; the transitions (B) are in the spectal range 5.0−10.0 eV, and the transitions (C) are in the spectal range 10.0−14.0 eV.

From the imaginary part of the dielectric function's dispersions $\varepsilon_2^{xx}(\omega)$, $\varepsilon_2^{yy}(\omega)$, and $\varepsilon_2^{zz}(\omega)$ the real part $\varepsilon_1^{xx}(\omega)$, $\varepsilon_1^{yy}(\omega)$, and $\varepsilon_1^{zz}(\omega)$ were calculated using Kramers−Kronig relations.[32] The results of the calculated $\varepsilon_1^{xx}(\omega)$, $\varepsilon_1^{yy}(\omega)$, and $\varepsilon_1^{zz}(\omega)$ are shown in Figure 3b. The calculated $\varepsilon_1^{xx}(0)$, $\varepsilon_1^{yy}(0)$ and $\varepsilon_1^{zz}(0)$ are presented in Table 2. Using the calculated dispersions of imaginary and real parts of the dielectric function one can evaluate other optical properties such as reflectivity spectra $R(\omega)$, absorption coefficients $I(\omega)$, refractive indices $n(\omega)$, loss function $L(\omega)$, and the conductivity $\sigma(\omega)$. We show these quantities in Figure 2c−i. The average reflectivity is given by

$$R(\omega) = \frac{R^{xx}(\omega) + R^{yy}(\omega) + R^{zz}(\omega)}{3}$$

Similar expressions can be written for the other optical properties. In Figure 3c, we compare the average measured reflectivity with the three components of the calculated reflectivity spectra. One can see a good agreement between theory and experiment in the sense that the calculations seem to reproduce most of the experimental structures in terms of location and peak heights. It is interesting that there is an abrupt reduction in the reflectivity spectrum at 12.5 eV for both the theoretical and experimental curves confirming the occurrence of a collective plasmon resonance. The depth of the plasmon minimum is determined by the imaginary part of the dielectric function at the plasma resonance and is representative of the degree of overlap between the interband absorption regions. The calculated absorption coefficient dispersion $I(\omega)$ is shown in Figure 3d. At higher energies (at around 12.5 eV), this crystal shows a fast increasing absorption. The calculated refractive index dispersions $n(\omega)$ are shown in Figure 3e. The calculated and measured values of $n^{xx}(0)$, $n^{yy}(0)$, and $n^{zz}(0)$ in comparison with the previous experimental and theoretical results are listed at Table 2. We note that at low energy KTP shows high refractive indices, which decrease at higher energies. KTP shows a considerable anisotropy that is important for second harmonic generation (SHG) and optical parametric oscillation (OPO) as it is defined by the phase-matching condition. The birefringence can be calculated from the linear response functions from which the anisotropy of the index of refraction is determined. The birefringence is the difference between the extraordinary and ordinary refraction indices, $\Delta n(\omega) = n_e(\omega) - n_o(\omega)$, where $n_o(\omega)$ is the index of refraction for an electric field oriented along the c-axis and $n_e(\omega)$ is the index of refraction for an electric field perpendicular to the c-axis. Figure 3f shows the birefringence $\Delta n(\omega)$ dispersion for this single crystal. It is clear that the birefringence is important only in the nonabsorbing spectral range, which is below the energy gap. We find that KTP crystal possesses a positive birefringence at zero energy equal to about 0.07 and 0.074 at 1.165 eV (1064 nm). We have compared our results with the available results see Table 2.

Electron energy loss spectroscopy (EELS) is a valuable tool for investigating various aspects of materials.[33] The plasmon losses corresponding to a collective oscillation of the valence electrons and their energies are related to the density of valence electrons. In the case of interband transitions, which consist mostly of plasmon excitations, the scattering probability for volume losses is directly connected to the energy loss function. In Figure 3g, the energy loss function is plotted in basal-plane and in direction of c-axis. There are other features in this spectrum in addition to the plasmon peak associated with interband transitions. The plasmon peak is usually the most intense feature in the spectrum and this is at energy where $\varepsilon_1(\omega)$ goes to zero. The energy of the maximum peak of $(-\varepsilon_1(\omega))^{-1}$ is observed at ~12.5 eV for $L^{xx}(\omega)$, $L^{yy}(\omega)$ and $L^{zz}(\omega)$, which are assigned to the energy of volume plasmon $\hbar\omega_p$. The calculated optical conductivity dispersion Im $\sigma(\omega)$ and Re $\sigma(\omega)$ are shown in Figure 3h,i, it also shows anisotropy between $\sigma^{xx}(\omega)$, $\sigma^{yy}(\omega)$, and $\sigma^{zz}(\omega)$. The optical conductivity (OC) is related to the frequency-dependent dielectric function $\varepsilon(\omega)$ as $\varepsilon(\omega) = 1 + [4\pi i\sigma(\omega)]/\omega$. The peaks in the optical conductivity spectra are determined by the electric-dipole transitions between the occupied states to the unoccupied states.

C. Nonlinear Optical Dispersion. The calculations of nonlinear optical properties are much more complicated than the linear one. The difficulties concern both the numeric and the physics, because more conduction bands and more k-points are required to achieve the maximum accuracy. Since the investigated crystal belongs to the space group $Pna2_1$, which possesses two crystallographic symmetry elements, and as a

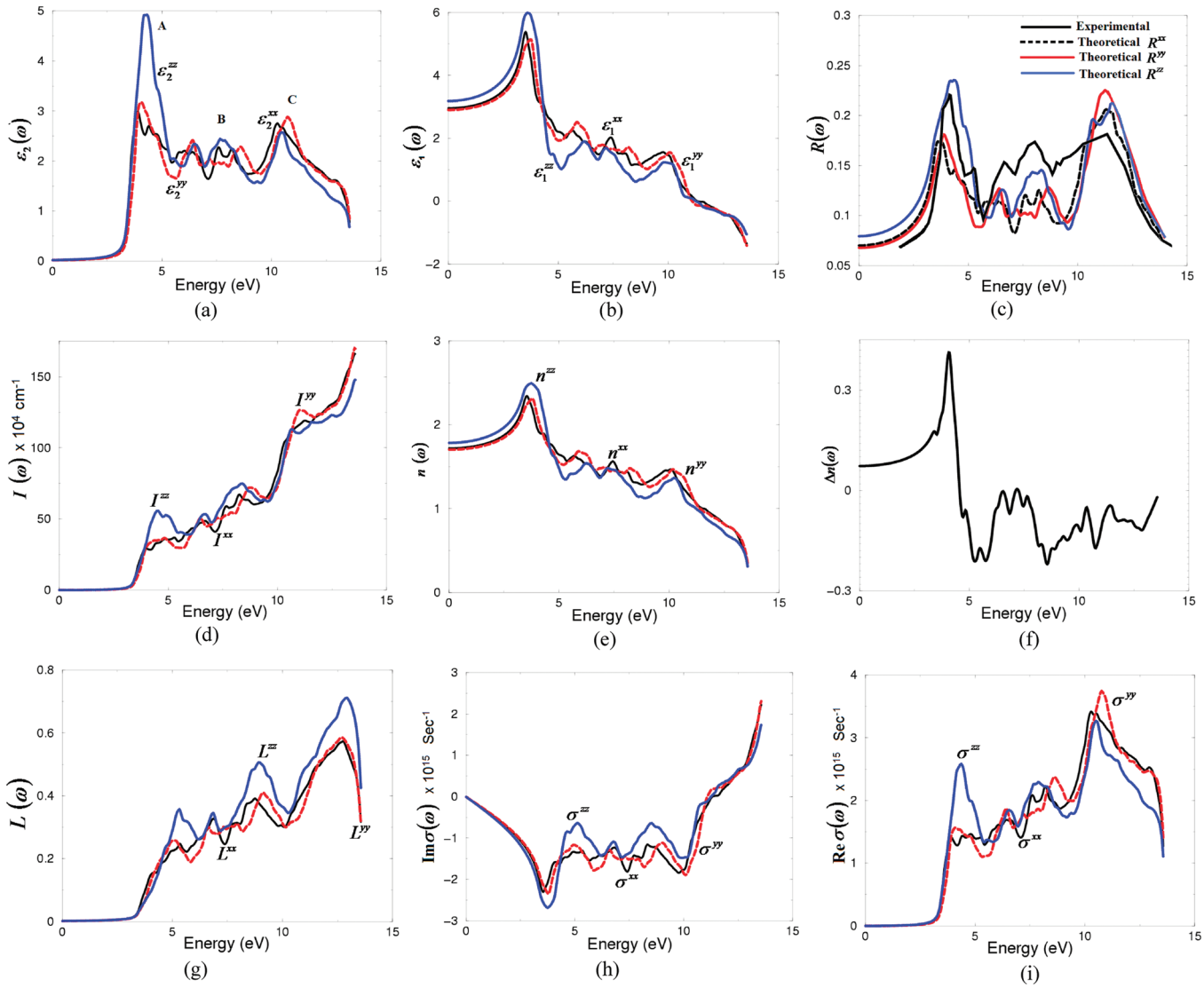

Figure 3. (a) Calculated $\varepsilon_2^{xx}(\omega)$ (black), $\varepsilon_2^{yy}(\omega)$ (red) and $\varepsilon_2^{zz}(\omega)$ (blue) spectra. (b) Calculated $\varepsilon_1^{xx}(\omega)$ (black), $\varepsilon_1^{yy}(\omega)$ (red), and $\varepsilon_1^{zz}(\omega)$ (blue) spectra. (c) Calculated $R^{xx}(\omega)$ (black), $R^{yy}(\omega)$ (red), and $R^{zz}(\omega)$ (blue) along with our measured total $R(\omega)$ (black). (d) Calculated absorption coefficient $I^{xx}(\omega)$ (black), $I^{yy}(\omega)$ (red), and $I^{zz}(\omega)$ (blue) spectrum. The absorption coefficient is 10^4 s^{-1} (e) Calculated refractive indices $n^{xx}(\omega)$ (black), $n^{yy}(\omega)$ (red), and $n^{zz}(\omega)$ (blue) spectrum. (f) Calculated birefringence $\Delta n(\omega)$. (g) Calculated loss function $L^{xx}(\omega)$ (black), $L^{yy}(\omega)$ (red), and $L^{zz}(\omega)$ (blue) spectrum. (h) Calculated imaginary part of the conductivity of $\sigma^{xx}(\omega)$ (black), $\sigma^{yy}(\omega)$ (red), and $\sigma^{zz}(\omega)$ (blue) spectrum. The optical conductivity is 10^{15} s^{-1}. (i) Calculated real part of the conductivity of $\sigma^{xx}(\omega)$ (black), $\sigma^{yy}(\omega)$ (red), and $\sigma^{zz}(\omega)$ (blue) spectrum. The optical conductivity is 10^{15} s^{-1}.

consequence we have several parameters that are equal to zero. As a result, the symmetry will allow only five nonzero component, namely, the 113, 232, 311, 322, and 333 components (1, 2, and 3 refer to the *x*, *y*, and *z* axes, respectively).[34] The complex second-order nonlinear optical susceptibility tensor $\chi_{ijk}^{(2)}(-2\omega;\omega;\omega)$ can be generally written as $\chi_{ijk}^{(2)}(\omega)$. The subscripts *i*, *j*, and *k* are the Cartesian indices. Accordingly, KTP possess the $\chi_{113}^{(2)}(\omega)$, $\chi_{232}^{(2)}(\omega)$, $\chi_{311}^{(2)}(\omega)$, $\chi_{322}^{(2)}(\omega)$, and $\chi_{333}^{(2)}(\omega)$ complex second-order nonlinear optical susceptibility tensors. The second-order nonlinear optical susceptibility is very sensitive to the scissors' correction. The scissors' correction has a profound effect on magnitude and sign of $\chi_{ijk}^{(2)}(\omega)$.[35,36] The well-known LDA and GGA underestimation of the energy band gaps may result in incorrect values of second-order nonlinear optical susceptibility tensor components since they are more sensitive to the band gaps than the linear-response values due to higher power energy differences in the denominators of the formulas of complex second-order nonlinear optical susceptibility tensors given in ref 29−31. To reduce the effect of the scissors' correction we have used the EV-GGA approach. It is well-known that the nonlinear optical properties are more sensitive to small changes in the band structure than the linear optical properties. Hence, any anisotropy in the linear optical properties is enhanced in the nonlinear spectra. This is attributed to the fact that the second harmonic response $\chi_{ijk}^{(2)}(\omega)$ involves the 2ω resonance in addition to the usual ω resonance. Both the ω and 2ω resonances can be further separated into interband and intraband contributions. The calculated imaginary part of the second harmonic generation susceptibility $\chi_{113}^{(2)}(\omega)$, $\chi_{232}^{(2)}(\omega)$, $\chi_{311}^{(2)}(\omega)$, $\chi_{322}^{(2)}(\omega)$, and $\chi_{333}^{(2)}(\omega)$ are shown in Figure 4a,b. A definite enhancement in the anisotropy on going from linear optical properties to the nonlinear optical properties is evident (Figure 4a,b). We can identify the origin of the spectral peaks in these figures as caused by $2\omega/\omega$ resonance peaks in the linear dielectric function. In Figure 4c, we show the $2\omega/\omega$ inter/intraband contributions to the total Im $\chi_{333}^{(2)}(\omega)$ of the dominant component $\chi_{333}^{(2)}(\omega)$. It is clear that the imaginary part of the second harmonic generation susceptibility is zero below half the energy band gap. The 2ω terms begin to contribute at energies $\sim 1/2E_g$ and the ω terms for energy values above E_g.

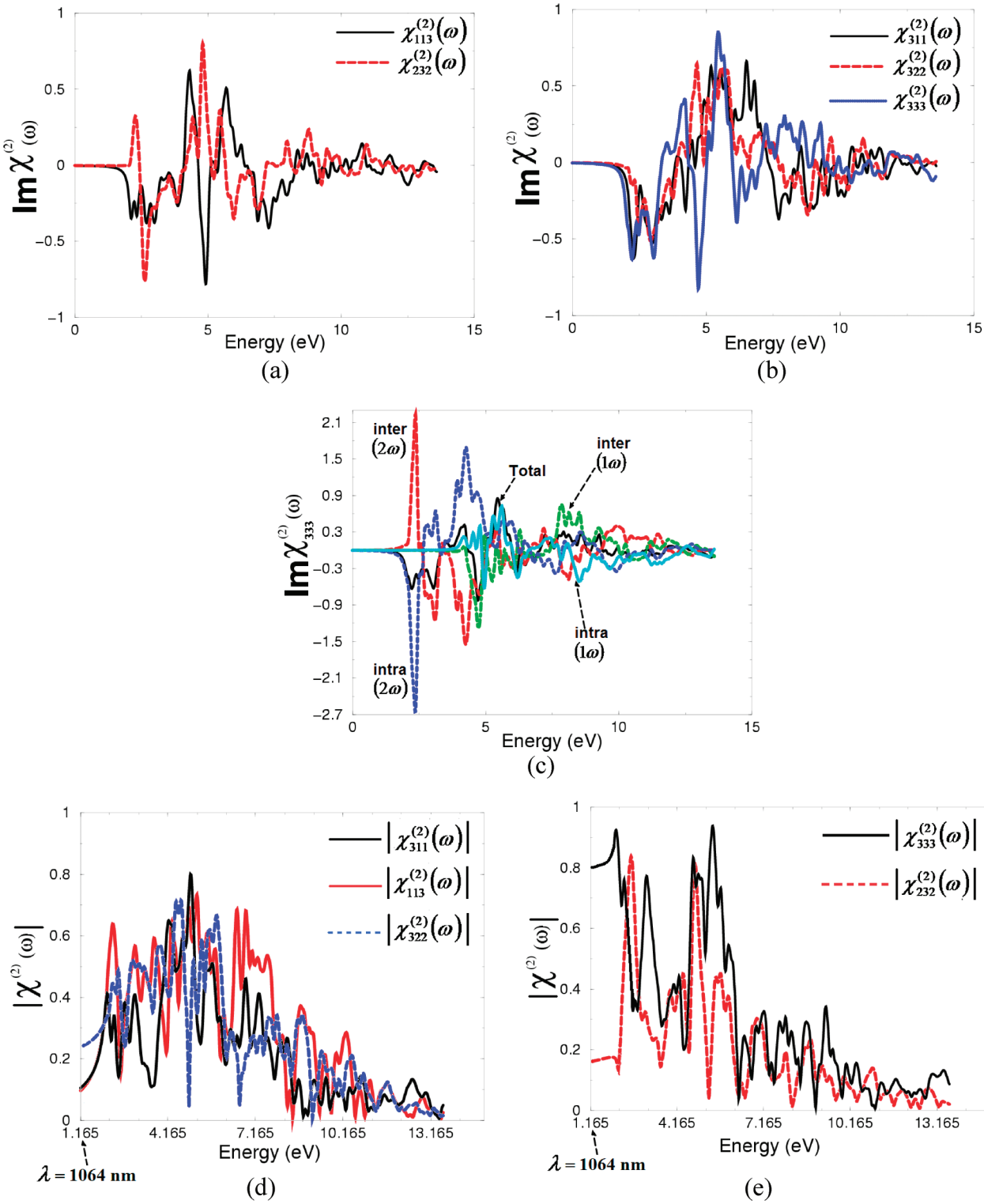

Figure 4. (a) Calculated Im $\chi^{(2)}_{113}(\omega)$ (black), and Im $\chi^{(2)}_{232}(\omega)$ (red) spectra. (b) Calculated Im $\chi^{(2)}_{311}(\omega)$ (black), Im $\chi^{(2)}_{322}(\omega)$ (red), and $\chi^{(2)}_{333}(\omega)$ (blue). (c) Calculated total Im $\chi^{(2)}_{333}(\omega)$ (black) spectrum along with the intra- $(2\omega)/(1\omega)$ (blue)/(cyan) and inter- $(2\omega)/(1\omega)$ (red)/(green) band contributions. (d) Calculated $|\chi^{(2)}_{311}(\omega)|$ (black), $|\chi^{(2)}_{113}(\omega)|$ (red) and $|\chi^{(2)}_{322}(\omega)|$ (blue) starting from 1.165 eV ($\lambda = 1064$ nm) to show the values of calculated $|\chi^{(2)}_{311}(\omega)|$, $|\chi^{(2)}_{113}(\omega)|$, and $|\chi^{(2)}_{322}(\omega)|$ at $\lambda = 1064$ nm. (e) Calculated $|\chi^{(2)}_{333}(\omega)|$ (black) and $|\chi^{(2)}_{232}(\omega)|$ (red) starting from 1.165 eV ($\lambda = 1064$ nm) to show the values of calculated $|\chi^{(2)}_{333}(\omega)|$ and $|\chi^{(2)}_{232}(\omega)|$ at $\lambda = 1064$ nm. All the $\chi^{(2)}_{ijk}(\omega)$ and $|\chi^{(2)}_{ijk}(\omega)|$ are multiplied by 10^{-7} in esu units.

At low spectral range ($\leq$1.6 eV), the SHG optical spectra is dominated by the 2ω contributions. Beyond 3.2 eV (values of the fundamental energy gaps) the major contribution comes from the ω term.

One would expect that the spectral structures in Im $\chi^{(2)}_{ijk}(\omega)$ could be understood from the structures in $\varepsilon_2(\omega)$. Unlike the linear optical spectra, the features in the SHG susceptibility are more difficult to identify from the band structure, because of the presence of 2ω and ω terms. But we can make use of the linear optical spectra to identify the different resonance leading to various features in the SHG spectra. The first structure in Im $\chi^{(2)}_{333}(\omega)$, between 1.7−5.0 eV, primarily originates from 2ω resonance and arises from the first structure in $\varepsilon_2(\omega)$. The second structure between 5.0−10.0 eV is associated with interference

TABLE 3: Calculated Total $|\chi^{(2)}_{ijk}(\omega)|$ in pm/V at $\lambda = 1064$ nm along with Our Measured Values of d_{ijk} Where 1 pm/V = 2.387 $\times$ 10^{-9} esu

tensor components	theory $\chi^{(2)}_{ijk}(\omega)$ in (pm/V)	theory $d_{ijk} = 0.5\chi^{(2)}_{ijk}(\omega)$in (pm/V)	our experiment at $\lambda = 1064$ nm in (pm/V)	other experiment at $\lambda = 1064$ nm in (pm/V)
total $\|\chi^{(2)}_{113}(\omega)\|$	4.0	$d_{15} = 2.0$	1.99	6.1,[b] 2.02 $\pm$ 0.07,[c] 1.9 $\pm$ 0.1,[e] 1.78 $\pm$ 0.2,[f] 1.91 $\pm$ 0.2,[h] 1.19 $\pm$ 0.08[i]
total $\|\chi^{(2)}_{232}(\omega)\|$	7.54	$d_{24} = 3.77$	3.81	7.6,[b] 3.9 $\pm$ 0.3,[d] 3.7 $\pm$ 0.2,[e] 3.37 $\pm$ 0.3,[f] 3.64 $\pm$ 0.47,[h] 2.37 $\pm$ 0.17[i]
total $\|\chi^{(2)}_{311}(\omega)\|$	5.4	$d_{31} = 2.7$	2.71	2.54,[a] 6.5,[b] 2.12 $\pm$ 0.07,[c] 2.2 $\pm$ 0.1,[e] 2.5 $\pm$ 0.5,[g] 2.54 $\pm$ 0.5,[h]
total $\|\chi^{(2)}_{322}(\omega)\|$	9.7	$d_{32} = 4.85$	4.79	4.35,[a] 5.0,[b] 3.75 $\pm$ 0.07,[c] 3.7 $\pm$ 0.1,[e] 4.4 $\pm$ 1.1,[g] 4.35 $\pm$ 0.4[h]
total $\|\chi^{(2)}_{333}(\omega)\|$	33.5	$d_{33} = 16.75$	16.65	16.9,[a] 13.7,[b] 15.4 $\pm$ 0.2,[c] 14.6 $\pm$ 1.0,[e] 17.4 $\pm$ 1.7,[f] 16.9 $\pm$ 3.3,[g] 16.9 $\pm$ 1.7,[h] 10.6 $\pm$ 7.5[i]

[a] Reference 5. [b] Reference 38. [c] Reference 3. [d] Reference 39. [e] Reference 40. [f] Reference 41. [g] Reference 42. [h] Reference 43. [i] Reference 44.

between a ω resonance and 2ω resonance and associated with high structure in $\varepsilon_2(\omega)$. The last structure from 10.0−14.0 eV is mainly due to ω resonance and associated with the tail in $\varepsilon_2(\omega)$.

The calculated $|\chi^{(2)}_{ijk}(\omega)|$ at $\lambda = 1064$ nm for all components in comparison with the previous results are listed in Table 3. It is well-known that the relationship between the second harmonic susceptibility coefficient d and the nonlinear susceptibility is $\chi^{(2)}_{ijk}(\omega) = 2d_{ijk} = d_{iJ}$[34,37] (here i takes values of 1,2,3 corresponding to x,y,z and J takes values 1,2,3,4,5,6 corresponding to xx,yy,zz,yz,xz,xy components, for example, xx takes the value 1, yy takes 2, zz takes 3, and so on). On the basis of this expression, we can compare our calculated $|\chi^{(2)}_{ijk}(\omega)|$ with the values of d_{15}, d_{24}, d_{31}, d_{32}, andd_{33}, which were obtained from our measurements at $\lambda = 1064$ nm. We have found a good agreement between the theoretically calculated and experimentally measured values in comparison with the previous measurements[3,5,38−44] as listed in Table 3. The damage threshold of the studied KTP crystal was equal to about 9.6 GW/cm^2, which indicates a good quality of the crystals. A major contribution to the nonlinear optical coefficients of the KTP crystal is attributed to the distortion of TiO_6 octahedra, which allows the dipolar excited states to mix with the bonding electronic states producing a strong hyperpolarizability on the Ti═O bonds.[5] We have calculated the microscopic second order hyperpolarizability, β_{333},[45] vector component along the dipole moment direction at $\lambda = 1064$ nm for the dominant component $\chi^{(2)}_{333}(\omega)$ and we find it to be 31.6 $\times$ 10^{-30} esu. The nonlinearity of KTP can be explained by the hyperpolarizability of the short Ti−O bonds, and in accordance with the idea that the hyperpolarizabilities are largest for polar covalent bonds.[15] In KTP, the microscopic second order hyperpolarizability β_{ijk} terms cumulatively yields a bulk observable second order susceptibility term, $\chi^{(2)}_{ijk}(\omega)$, which in turn is responsible for the high SHG response of KTP.[46] The superior nonlinear optical properties of KTP crystal originate mainly from the distorted TiO_6 octahedra. The extremely short Ti−O bond of the distorted TiO_6 octahedra possesses a strong covalent bond character and charge can easily transferred between the Ti and O atoms, and it is very susceptible to the applied optical field of laser.[5]

IV. Conclusions

We have performed calculations of the linear and nonlinear optical properties of potassium titanyl phosphate $KTiOPO_4$ (KTP) using the state-of-the-art FP-LAPW method. Our calculated energy gap (direct) using EV-GGA is 3.1 eV. This is in good agreement with the measured gap of 3.2 eV. We have found a good agreement between the measured and calculated reflectivity spectra. The spectral features of $\varepsilon_2(\omega)$ are discussed and analyzed in terms of the calculated band structure. We have found that there is a considerable anisotropy between the various components of the optical properties. KTP possesses positive birefringence at zero energy of about 0.07. Our calculated and measured SHG susceptibilities shows good agreement. In addition, the second order hyperpolarizability, β_{333}, vector component along the dipole moment direction, has been calculated for the dominant component $\chi^{(2)}_{333}(\omega)$ at $\lambda = 1064$ nm and we find it to be 31.6 $\times$ 10^{-30} esu. A major contribution to the nonlinear optical coefficients of the KTP crystal is attributed to the distorted TiO_6 octahedron which allows the dipolar excited states to mix with the bonding electronic states producing a strong hyperpolarizability on the Ti−O bonds.

Acknowledgment. This work was supported from the institutional research concept of the Institute of Physical Biology, UFB (No.MSM6007665808), the program RDI of the Czech Republic, the project CENAKVA (No. CZ.1.05/2.1.00/01.0024), Grant 152/2010/Z of the Grant Agency of the University of South Bohemia, and The School of Microelectronic Engineering, University Malaysia Perlis (UniMAP), Block A, Kompleks Pusat Pengajian, 02600 Arau Jejawi, Perlis, Malaysia.

References and Notes

(1) Tordjman, I. I.; Masse, R.; Guitel., J. C. *Z. Kristallogr.* **1974**, *139*, 103–115.
(2) Zumsteg, F. C.; Bierlein, J. D.; Gier, T. E. *J. Appl. Phys.* **1976**, *47*, 4980–4985.
(3) Pack, M. V.; Armstrong, D. J.; Smith, A. V. *Appl. Opt.* **2004**, *43*, 3319.
(4) Stucky, G. D.; Phillip, M. L. F.; Gier, T. E. *Chem. Mater.* **1989**, *1* (5), 492.
(5) Zhang, K.; Wang, X. *Chin. Sci. Bull.* **2001**, *46*, 2028–2036.
(6) Lowther, J. E.; Manyum, P.; Suebka, P. *Phys. Status Solidi B* **2005**, *242*, 1392–1398.
(7) (a) Baumert, J. C.; Schellenberg, F. M.; Risk, W. P.; Bjorklund, G. C. *Appl. Phys. Lett.* **1987**, *51*, 2192. (b) Risk, W. P.; Baumert, J. C.; Bjorklund, G. C.; Schellenberg, F. M.; Lenth, W. *Appl. Phys. Lett.* **1988**, *52*, 85.
(8) Zhang, R.; Lu, F.; Lian, J.; Liu, H.; Liu, X.; Lu, Q.; Ma, H. *Opt. Express* **2008**, *16*, 6768–6773.
(9) Pena, A.; Finizo, S. D.; Trifonov, T.; Carvajal, J. J.; Aguilo, M.; Pallares, J.; Rodriguez, A.; Alcubilla, R.; Marsal, L. F.; Diaz, F.; Martorell, J. *Adv. Mater.* **2006**, *18*, 2220–2225.
(10) Norberg, S. T. *Annual Report of the Ceramics Research Laboratory Nagoya Institute of Technology*; **2005**, *4*, 15−20.
(11) Pysher, M.; Bloomer, R.; Kaleva, M. G.; Roberts, T. D.; Battle, P.; Pfister, O. *Opt. Lett.* **2009**, *34*, 256–258.
(12) Kugel, G. E.; Brehat, F.; Wyncke, B.; Fontana, M. D.; Marnier, G.; Carabatos-Nedelec, C.; Mangin, J. *J. Phys. C: Solid State Phys.* **1988**, *21*, 5565–5583.
(13) Jiang, Q.; Thomas, P. A.; Walker, D.; Hutton, K. B.; Ward, R. C. C.; Pernot, P.; Baruchel, J. *J. Phys. D: Appl. Phys.* **2003**, *36*, 1236–1241.
(14) Hansen, N. K.; Protas, J.; Marnier, G. *Acta. Cryst. B* **1991**, *47*, 660–672.
(15) Thomas, J. M.; Renshaw, G. D. *Trans. Faraday Soc.* **1968**, *61*, 791.

(16) Thomas, P. A.; Glazer, A. M.; Watts, B. E. *Acta Cryst. B* **1992**, *48*, 401.
(17) Reid, D. T.; Ebrahimzadeh, M.; Sibbett, W. *J. Opt. Soc. Am. B* **1995**, *12*, 2168.
(18) Masse, R.; Grenier, J. C. *Bull. Soc. Fr. Mineral. Cristallogr.* **1971**, *94*, 437.
(19) Belt, R. F.; Gashurov, G.; Liu, Y. S. *Laser Focus* **1985**, 110.
(20) Fan, T. Y.; Huang, C. E.; Hu, B. Q.; Eckhardt, R. C.; Fan, Y. X.; Byer, R. L.; Feigelson, R. S. *Appl. Opt.* **1987**, *26*, 2391.
(21) Ballman, A. A.; Brown, H.; Olson, D. H.; Rice, C. E. *J. Cryst. Growth* **1986**, *75*, 390.
(22) Bierlein, J. D.; Vanherzeele, H.; Ballman, A. A. *Appl. Phys. Lett.* **1989**, *54*, 783.
(23) Jerphagnon, J.; Kurtz, S. K. *J. Appl. Phys.* **1970**, *41*, 1667–1681.
(24) Shoji, I.; Kondo, T.; Kitamoto, A.; Shirane, M.; Ito, R. *J. Opt. Soc. Am. B* **1997**, *14*, 2268. Hagimoto, K.; Mito, A. *Appl. Opt.* **1995**, *34*, 8276. Roberts, D. A. *IEEE J. Quantum Electron.* **1992**, *28*, 2057.
(25) Blaha, P.; Schwarz, K.; Madsen, G. K. H.; Kvasnicka, D.; Luitz, J., *WIEN2K, "an Augmented Plane Wave + Local orbitals program for calculating crystal properties*, Karlheinz Schwarz, Techn. Universitat, Wien, Austria, 2001, ISBN 3−9501031−1-2.
(26) Perdew, J. P.; Burke, K.; Ernzerhof, M. *Phys. Rev. Lett.* **1996**, *77*, 3865.
(27) Dufek, P.; Blaha, P.; Schwarz, K. *Phys. Rev. B* **1994**, *50*, 7279.
(28) Engel, E.; Vosko, S. H. *Phys. Rev. B* **1993**, *47*, 13164.
(29) (a) Sharma, S.; Dewhurst, J. K.; Ambrosch-Draxl, C. *Phys. Rev. B* **2003**, *67*, 165332. (b) Sharma, S.; Ambrosch-Draxl, C. *Phys. Scr. T* **2004**, *109*, 128.
(30) Reshak, A. H. Ph.D. Thesis, Indian Institute of Technology-Rookee, India, 2005.
(31) (a) Rashkeev, S. N.; Lambrecht, W. R. L. *Phys. Rev. B* **2001**, *63*, 165212. (b) Rashkeev, S. N.; Lambrecht, W. R. L.; Segall, B. *Phys. Rev. B* **1998**, *57*, 3905.
(32) Tributsch, H. *Z. Naturforsch. A* **1977**, *32A*, 972.
(33) Loughin, S.; French, R. H.; De Noyer, L. K.; Ching, W.-Y.; Xu, Y.-N. *J. Phys. D: Appl. Phys.* **1996**, *29*, 1740.
(34) Boyd., R. W. *Principles of Nonlinear Optics*; Academic Press: NY, 1982; p 420.
(35) Reshak, A. H.; Auluck, S. *Physica B* **2007**, *388*, 34–42.
(36) Reshak, A. H.; Auluck, S.; Kityk, I. V. *Appl. Phys. A.* **2008**, *91*, 451–457.
(37) Encyclopedia of Laser Physics and Technology. http://www.rp-photonics.com/nonlinear_polarization.html (Oct 2010).
(38) CASTECH. http://www.castech-us.com/casktp.htm (Oct 2010).
(39) Alford, W. J.; Smith, A. V. *J. Opt. Soc. Am. B* **2001**, *18*, 524.
(40) Kondo, Shoji T.; Kitamoto, A.; Shirane, M.; Ito, R. *J. Opt. Soc. Am. B* **1997**, *14*, 2268.
(41) Anema, A.; Rasing, T. *Appl. Opt.* **1997**, *36*, 5902.
(42) Cheng, L. K.; Cheng, L. T.; Galperin, J.; Hotsenpiller, P. A. M.; Bierlein, J. D. *J. Cryst. Growth* **1994**, *137*, 107.
(43) Vanherzeele, H.; Bierlein, J. D. *Opt. Lett.* **1992**, *17*, 982.
(44) Boulanger, B.; Feve, J. P.; Marnier, G.; Menaert, B. *Pure Appl. Opt.* **1998**, *7*, 239.
(45) Boyd, R. W. *Nonlinear optics*, 3rd ed.; Acadmic Press: New York, 2008.
(46) Harrison, W. T. A.; Phillips, M. L. F.; Stucky, G. D. *Chem. Matter.* **1995**, *7*, 1849–1856.

JP1072878